

# Evidence for Fe $K_{\alpha}$ line and soft X-ray lag in NGC 7456 ULX-1

Samaresh Mondal,<sup>1\*</sup> Agata Rózańska<sup>1</sup>, Barbara De Marco<sup>2</sup> and Alex Markowitz<sup>1,3</sup>

<sup>1</sup>*Nicolaus Copernicus Astronomical Center, Polish Academy of Sciences, ul. Bartycka 18, PL-00-716 Warsaw, Poland*

<sup>2</sup>*Department de Física, EEBE, Universitat Politècnica de Catalunya, Av. Eduard Maristany 16, E-08019, Barcelona, Spain*

<sup>3</sup>*University of California, San Diego, Center for Astrophysics and Space Sciences, MC 0424, La Jolla, CA, 92093-0424, USA*

Accepted XXX. Received YYY; in original form ZZZ

## ABSTRACT

We report the first detection of a Fe  $K_{\alpha}$  line and soft X-ray lag in the ultraluminous X-ray source (ULX) NGC 7456 ULX-1. The *XMM-Newton* spectra show the presence of the 6.4 keV Fe line at  $2.6\sigma$  confidence and an upper limit on the FWHM of 32900 km s<sup>-1</sup>. Assuming that the line arises by reflection from a Keplerian disk, it must originate beyond  $85r_g$  from the compact object. As a result of Fourier timing analysis we found that the soft X-ray photons lag behind the hard X-ray photons with a  $\sim 1300$  s delay. The covariance spectra indicate that the hard spectral component is responsible for the correlated variability and the soft X-ray lag. This is the second ULX in which a Fe  $K_{\alpha}$  line is found, the fifth with a soft X-ray lag, and the first with both features detected.

**Key words:** stars: black holes, X-rays: binaries, X-rays: individual (NGC 7456 ULX-1)

## 1 INTRODUCTION

Ultraluminous X-ray (ULX) sources are off-nuclear point sources with X-ray luminosity exceeding the Eddington luminosity of a  $10 M_{\odot}$  black hole (BH) ( $L_X > 10^{39}$  erg s<sup>-1</sup>). ULXs are prime candidates in which to study super-Eddington accretion flows, as a few of them are identified to contain a neutron star (NS) (Bachetti et al. 2014; Fürst et al. 2016; Israel et al. 2017a,b; Brightman et al. 2018; Carpano et al. 2018; Sathyaprakash et al. 2019; Rodríguez Castillo et al. 2020), with the prospect of stellar-mass BHs existing in many others (Mondal et al. 2020, 2021).

Most ULXs do not show strong X-ray variability, (Heil et al. 2009) and those which do show it, lack short time scale (< ks) variability compared to X-ray binaries (XRBs) and active galactic nuclei (AGN). It has been suggested that the short time scale variability is suppressed due to the interaction of photons coming from the inner hotter region with the outflowing material. X-ray variability studies made for a few ULXs, using various approaches, resulted in discoveries of quasi-periodic oscillations (Strohmayer & Mushotzky 2003), linear rms-flux relations (Heil & Vaughan 2010; Hernández-García et al. 2015), and time-lag analyses (Heil & Vaughan 2010; De Marco et al. 2013b). However, variability studies of ULXs are hampered by low count rates which necessitate long exposure times to recover their statistical properties. The detection of linear rms-flux relations in NGC 5408 X-1 (Heil & Vaughan 2010), NGC 6946 X-1 (Hernández-García et al. 2015) and M51 ULX-7 (Earnshaw et al. 2016) may suggest a common origin of X-ray variability among ULXs, XRBs, and AGNs.

Walton et al. (2011) reported the presence of four ULXs in NGC 7456 based on a 2005 *XMM-Newton* observation. Recently, Pintore et al. (2020) analyzed a deep *XMM-Newton* observation from 2018 and detected an additional ULX (ULX-5) in NGC 7456. Pintore et al. (2020) performed spectral and temporal analysis of all ULXs

hosted in this galaxy and found that ULX-1 is the brightest and most variable one. Therefore, in this paper we use the same *XMM-Newton* observation of ULX-1, with a duration of  $\sim 92$  ks, to perform detailed studies of its X-ray variability properties. We report new findings obtained from spectral-timing analysis of this bright ULX.

## 2 DATA REDUCTION

We reduced the *XMM-Newton* (Jansen et al. 2001) observation of NGC 7456 (ObsID 0824450401, 2018 May 18); its 92.4 ks duration makes it the longest observation for reliable spectral and timing analysis. The observation was processed using *XMM-Newton* Science Analysis System (SASv16.0.0) following standard procedures. The good exposure time after screening was 82.1 ks. We only selected events with PATTERN $\leq 4$  and PATTERN $\leq 12$ , respectively, for the EPIC-pn and EPIC-MOS cameras. Source spectra and lightcurves were obtained from a source circular region of  $40''$ . Background were extracted from regions of  $60''$ , confirmed with the `edetect_chain` task to devoid of point sources and avoiding Cu ring on pn-CCD chip. The response matrices and auxiliary files were generated using the SAS tasks `rmfgen` and `arfgen`, respectively.

As a first step, we used optimal spectral binning (Kaastra & Bleeker 2016) in the aim to detect the Fe line. But it turned out that the continuum was binned very much up to 95 counts per bin, while the line region at 6.4 keV had the same statistic as 20 counts per energy bin. Since we require high energy resolution for the continuum to constrain potential continuum curvature we use moderate binning. Therefore, for better constrains on the line and continuum parameters we use binning of 20 counts per energy bin. The lightcurves were extracted using 10 s time bins and background corrected using the SAS task `epiclccorr`. For our timing analysis we used lightcurves from the EPIC-pn detector only as it has nearly three times higher effective area than each MOS detector.

\* E-mail: smondal@camk.edu.pl (SM)

### 3 RESULTS

#### 3.1 Time-averaged spectral analysis

We first perform a time-averaged spectral fit to obtain the spectral decomposition and the unabsorbed luminosity of the source. [Pintore et al. \(2020\)](#) performed detailed spectral analysis of the same data, and found that the broad band continuum can be fitted equally well by a number of two component models similar to many other ULXs. In these models there is a the multi-color disk (MCD) component which peaks in the soft X-ray band (0.3–1 keV) plus an additional component for the hard X-ray photons, either a thermal Comptonization ([Gladstone et al. 2009](#)) or a hotter black body. Here we focus on a model comprised of MCD (`diskbb`) plus thermal Comptonization (`nthcomp`). For spectral fitting we used `xSPEC` v12.11.1 ([Arnaud 1996](#)).

Fitting with `diskbb` plus `nthcomp` reveals an excess near 6.4 keV from Fe  $K_{\alpha}$  emission. This is illustrated in the data to model ratio plot in the middle panel of Fig. 1. Adding an extra Gaussian component to the continuum model improved the fit by  $|\Delta\chi^2|=8$  for three fewer degrees of freedom. To estimate the statistical significance of the detection we performed Monte Carlo simulations using the tool `mc_sig`<sup>1</sup> in ISIS ([Houck & Denicola 2000](#)) which can take into account multiple data sets with different response files for simultaneous analysis. The line is inconsistent with photon noise at 99.0% confidence level (keeping all line parameters free) or  $> 99.0\%$  (keeping line centroid and width  $\sigma$  frozen at best-fit values). We also checked that the Akaike Information Criterion (AIC, [Akaike 1974](#)) and Bayesian information criterion (BIC, [Schwarz 1978](#)) give lower values, after adding Gaussian component, by  $|\Delta\text{AIC}|=1.5$  and  $|\Delta\text{BIC}|=125$ .

Our best-fit model for ULX-1 in NGC 7456 is composed of an absorbed MCD plus thermal Comptonization plus a narrow Gaussian at 6.4 keV for the Fe  $K_{\alpha}$  emission: `constant*tbabs*(diskbb+nthcomp+gauss)`, as shown in Fig. 1 bottom panel. The constant term is used for cross calibration uncertainties, and we keep it free for different detectors but fixed to unity for EPIC-pn. The fitting parameters with 90% confidence error are:  $N_{\text{H}} = 7.21^{+1.9}_{-1.7} \times 10^{20} \text{ cm}^{-2}$ ,  $kT_{\text{in}} = 0.23^{+0.03}_{-0.02} \text{ keV}$ ,  $\Gamma = 1.70^{+0.35}_{-0.24}$ ,  $kT_{\text{e}} = 1.0 \pm 0.6 \text{ keV}$ ,  $E_{\text{gauss}} = 6.44^{+0.29}_{-0.20} \text{ keV}$ ,  $\sigma = 0.16 \pm 0.14 \text{ keV}$ ,  $N_{\text{gauss}} = 4.4^{+3.3}_{-2.5} \times 10^{-7} \text{ ph cm}^{-2} \text{ s}^{-1}$ , and  $\chi^2/dof = 389.78/373$ . The resulting equivalent width (EW) of the line is  $2000^{+1500}_{-1100} \text{ eV}$ . A contour plot of line intensity vs. electron temperature of `nthcomp` model component is shown in Fig. 2, supporting that the line is detected at  $2.6\sigma$  significance.

The unabsorbed 0.3–10 keV flux is  $2.28 \times 10^{-13} \text{ erg s}^{-1} \text{ cm}^{-2}$ . Assuming a distance to the host galaxy of 15.7 Mpc ( $z = 0.00364$ ; [Tully et al. 2016](#)), the source unabsorbed luminosity (0.3–10 keV) is  $6.74 \times 10^{39} \text{ erg s}^{-1}$  and the line rest-frame energy is  $(1+z)E_{\text{gauss}} = 6.44 \text{ keV}$ . The upper panel of Fig. 1 shows the spectral decomposition of the unfolded model. The soft (`diskbb`) and hard (`nthcomp`) component dominates mostly below and above 1.3 keV, respectively.

#### 3.2 Power spectra and fractional variability

NGC 7456 ULX-1 was recognized by [Pintore et al. \(2020\)](#) as highly variable, and here we perform a detailed exploration of it's variability. The top panel of Fig. 3 shows the total band (0.3–10 keV) lightcurve, where the variability on time scales of ks is visible. The lightcurves

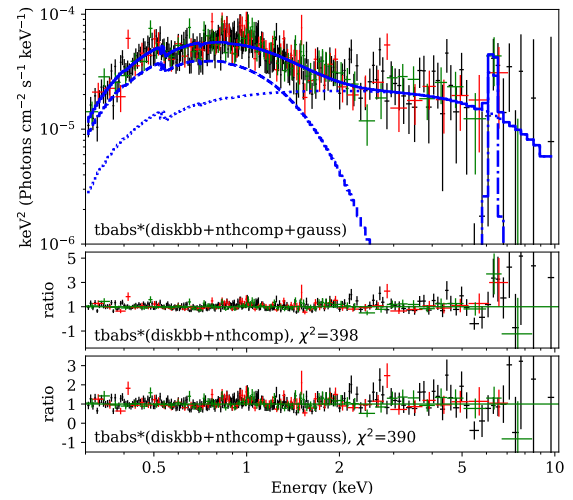


**Figure 1.** The top panel shows the unfolded time-averaged continuum spectrum, composed of a MCD (dashed curve) plus thermal Comptonization (dotted curve) plus a narrow Gaussian (dotted-dash curve), while the total model is shown by the continuous line. Note the excess at 6.4 keV from Fe  $K_{\alpha}$  emission in the middle panel. The black, red and green data points are from the EPIC-pn, MOS1 and MOS2 detectors, respectively.

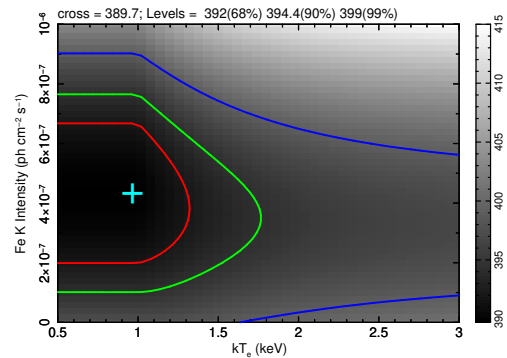


**Figure 2.** The  $\chi^2$  contour plot of line intensity vs. electron temperature. The red, green and blue lines show the confidence levels at 68% ( $\Delta\chi^2 = 2.3$ ), 90% ( $\Delta\chi^2 = 4.6$ ) and 99% ( $\Delta\chi^2 = 9.2$ ), respectively. The color bar shows the values of  $\chi^2$ .

of the selected soft (0.3–1 keV) and hard (1–10 keV) band are shown in the bottom panel of Fig. 3. These lightcurves have been smoothed using a Gaussian kernel with a width of 500 s to reduce the random fluctuations due to Poisson noise. One can see there is a slight delay between the peaks of the two bands.

As the lightcurves show enhanced variability, we performed Fourier timing analysis to estimate power spectral density functions (PSD). The PSDs were computed by averaging over duration of  $\sim 40$  ks and then logarithmically re-binning by a factor of 1.24. The top panel of Fig. 4 shows the PSDs in fractional rms squared normalization for both soft and hard bands. There is no obvious visual evidence for a power-law break. Therefore, we fitted the PSDs using a simple power law plus a constant for the Poisson noise which dominated at high frequency:  $A(f/10^{-4}\text{Hz})^{-\beta} + C$ , where  $A$  is the power at  $10^{-4} \text{ Hz}$ . The fit parameters, with  $1\sigma$  errors, for the soft band are  $A = 359.56 \pm 30.11$ ,  $\beta = 2.03 \pm 0.09$ ,  $C = 35.82 \pm 9.84$ ; for the hard band,  $A = 430.44 \pm 13.43$ ,  $\beta = 2.56 \pm 0.03$ ,  $C = 152.33 \pm 4.81$ . The Poisson noise starts to dominate above  $\sim 0.5 \text{ mHz}$ . The PSD fitting reveals that the hard band has more high-frequency variability power than the soft band at 0.1–0.3 mHz, which means the hard band is

<sup>1</sup> [https://www.sternwarte.uni-erlangen.de/gitlab/remeis/isisscripts/-/blob/master/src/misc/simulation/mc\\_sig.sl](https://www.sternwarte.uni-erlangen.de/gitlab/remeis/isisscripts/-/blob/master/src/misc/simulation/mc_sig.sl)

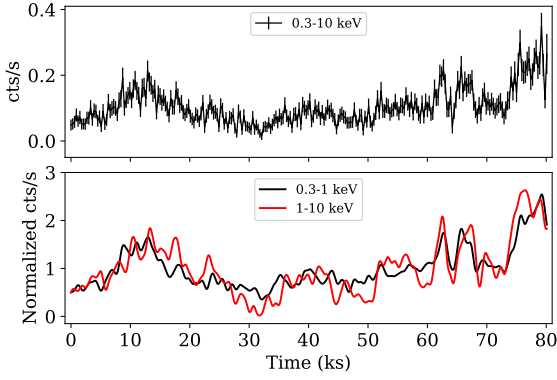


**Figure 3.** The top panel shows the background subtracted EPIC-pn lightcurve in the 0.3–10 keV energy band, with bin size  $\Delta t = 300$  s. A time shift between the peaks of the soft (0.3–1 keV) and hard (1–10 keV) bands is visible in the bottom panel.

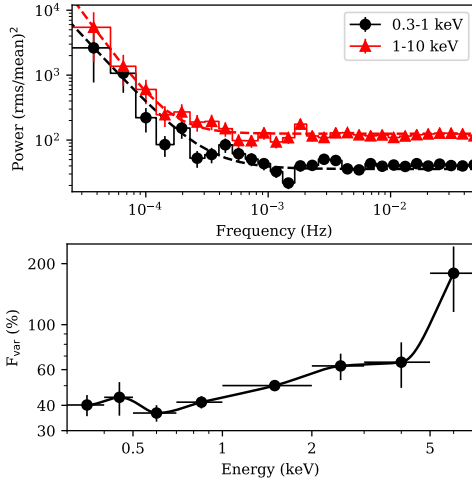


**Figure 4.** Top panel: PSDs for the soft and hard bands. The dashed lines show the best fits for a model composed of a simple power law plus a constant. Bottom panel: fractional variability as a function of energy computed in the frequency interval  $[0.25\text{--}5] \times 10^{-4}$  Hz. The points have been connected with a monotonic cubic interpolation to guide the eye.

more variable on short time scales than the soft band. This is expected considering that hard photons come from compact regions closer to the central object than soft photons, thus producing more rapid variability.

To check if the variability really increases with energy we compute the fractional variability,  $F_{\text{var}}$  (Edelson et al. 2002; Vaughan et al. 2003), from lightcurves in eight different energy bands (0.3–0.4, 0.4–0.5, 0.5–0.7, 0.7–1, 1–2, 2–3, 3–5, and 5–7 keV). The signal to noise ratio above 7 keV is too low for meaningful energy-dependent analysis constraints. We used time bins of 1000 s because the Poisson noise dominates on shorter timescales, corresponding to frequencies  $> 0.5$  mHz (Fig. 4 upper panel). This allowed us to sample the red-noise dominated part of the PSD. The lightcurves are chopped into two segments of 40 ks in length. Then  $F_{\text{var}}$  was computed separately for each segment and averaged over the two segments.  $F_{\text{var}}$  thus gives the power spectra integrated over the frequency between  $2.5 \times 10^{-5}$  Hz to 0.5 mHz. The bottom panel of Fig. 4 shows  $F_{\text{var}}$  increasing as a function of energy above 1 keV.  $F_{\text{var}}$  is almost constant (within the errors) from 0.3 keV up to 1 keV. This may indicate that softer photons come from a single emitting region.

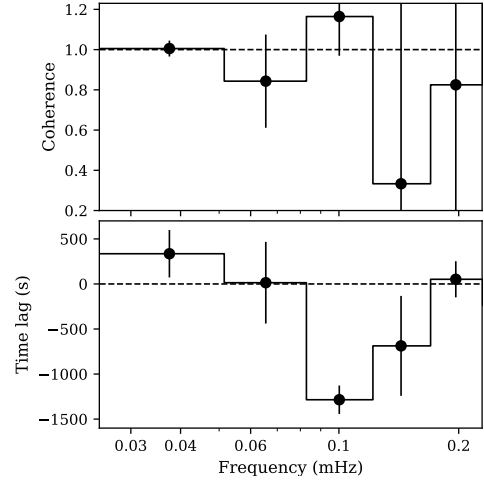


**Figure 5.** The coherence (top panel) and time lag (bottom panel) versus frequency plot for the un-smoothed lightcurves. A negative lag means that soft photons lag hard photons.

### 3.3 Time lag analysis

To confirm and quantify the delay shown in Fig. 3, we measured the frequency-dependent time lag between the (un-smoothed) soft and the hard band lightcurves, following the procedure outlined in Uttley et al. (2014). First we chopped the soft and hard band lightcurves into two segments  $\sim 40$  ks long. Then we computed the cross spectrum from each individual segment. Next, we averaged the cross spectra over the two segments, and the averaged cross spectrum was re-binned logarithmically using a factor of 1.24. The time lag is given by the formula  $\tau = \phi(f)/2\pi f$ , where  $\phi(f)$  is the phase lag obtained from the re-binned averaged cross spectrum. We used the modulus of the cross spectrum to compute the coherence, a measurement of the level of linear correlation between the two light curves (Vaughan & Nowak 1997). Fig. 5 shows the frequency-dependent coherence (top panel) and time lag (bottom panel). The noise corrected coherence and its error are computed using Eq. 8 in Vaughan & Nowak (1997). The coherence is consistent with unity after correction for the Poisson noise, meaning the variations in one band are linearly well-correlated with variations in the other band (Vaughan & Nowak 1997). We follow the convention that the negative lag means that the soft X-ray photons lag behind the hard X-rays and vice versa for positive lag. We observe a negative lag at frequencies above  $\sim 0.07$  mHz. At low frequencies lags are consistent with a hard lag as we previously saw after smoothing the lightcurves with a Gaussian kernel, and the amplitude of this lag is  $336 \pm 263$  s in the frequency bin 0.025–0.05 mHz. To prove that the soft lag is not caused by the Poisson noise, we simulated lightcurves using the Timmer & Koenig (1995) algorithm, generating coherent soft and hard band light curves with identical PSD properties, Poisson noise, and count rates to those measured for the real data. Only 14/1000 trials yielded lags more negative than  $-1300$  s at 0.1 mHz, rejecting the notion of the lag being due to photon noise at  $2.4\sigma$  confidence.

Next, the lag energy spectrum was obtained (see Fig. 6) by computing the cross spectra between the reference band and adjacent energy bands. We used 0.3–0.7 keV as the reference band. Furthermore, the lag was estimated from the resultant cross spectra which was averaged over frequencies where we detected the soft lag with high coherence in Fig. 5, roughly  $[0.7\text{--}1.2] \times 10^{-4}$  Hz. The lags have not been shifted, so zero lag means there is no time delay between that band and the reference band. Similarly a negative lag means the

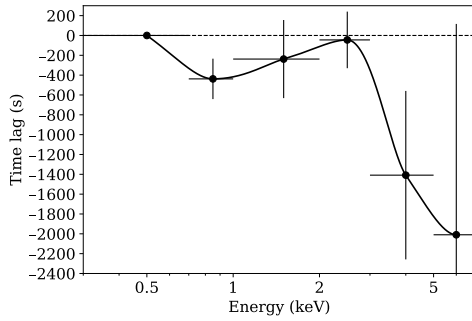


**Figure 6.** The lag-energy spectra in the frequency interval  $[0.7\text{--}1.2]\times 10^{-4}$  Hz. The points have been connected with a monotonic cubic interpolation to guide the eye.

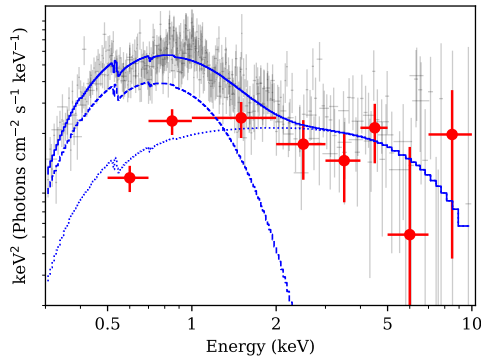


**Figure 7.** The figure shows the covariance spectrum (red data points) computed over the frequency range  $[0.5\text{--}1.5]\times 10^{-4}$  Hz, compared with the time-averaged energy spectrum (light gray points). The Y-axis is scaled arbitrarily to compare the shape of the covariance spectra with the time-averaged spectrum. The covariance spectrum follows the shape of the Comptonization component (dotted curve).

bin leads the reference band. The lag shows a sharp drop above 3 keV.

We further computed the frequency-dependent covariance spectrum to check which component of the energy spectrum is associated with the correlated variability. The covariance is computed following the prescription outlined in [Wilkinson & Uttley \(2009\)](#) in a similar frequency interval (0.05–0.15 mHz) as the lag-energy spectrum. Then the covariance spectrum was loaded into *XSPEC* and modeled with an absorbed power law with column density fixed to  $5.84\times 10^{20}\text{ cm}^{-2}$ , obtained from the time averaged continuum fitting. The unfolded covariance spectrum is shown in Fig. 7 (red points; covariance is shifted along the Y axis) together with the time averaged spectrum for comparison. It is apparent that the covariance spectrum is harder than the time averaged spectrum and seems to follow the shape of the *n*thcomp component. The covariance spectrum provides independent confirmation about which spectral component is responsible for the observed correlated variability.

#### 4 DISCUSSION AND CONCLUSION

We report the detection of an Fe  $K_{\alpha}$  line in ULX-1 in NGC 7456. The 0.3–10 keV mean spectrum is broadly described by a two-component model where the soft component dominates in the 0.3–1 keV band and the hard component in the 1–10 keV band. The source is in the

ultraluminous soft state ([Gladstone et al. 2009](#); [Sutton et al. 2013](#)) in which the soft component peaks over the hard component (Fig. 1).

The Fe  $K_{\alpha}$  line is detected at  $2.6\sigma$  confidence, but the line width is poorly constrained, and we obtain an upper limit on the width  $\sigma < 300$  eV. The full width at half-maximum of velocity broadening is  $v_{\text{FWHM}} < 32900\text{ km s}^{-1}$ . In ULXs the geometry of accreting gas is still unknown. For simplicity, we will assume  $\langle v^2 \rangle = v_{\text{FWHM}}^2$  in ULXs. Then we use  $\langle v^2 \rangle = \frac{GM}{R}$  to infer the distance of the line-emitting gas from the central compact object under the assumption that the line-emitting gas is in Keplerian motion around the central compact object. We obtain a distance of  $R = \frac{c^2}{\langle v^2 \rangle} r_g > 85r_g$ .

So far, Fe  $K_{\alpha}$  emission has not been detected in many ULXs, and NGC 7456 ULX-1 would be the second ULX source where this line is detected. Here, the line has an EW of  $2000^{+1500}_{-1100}$  eV, described in Sec. 3.1. Previously, an Fe  $K_{\alpha}$  line was detected in M82 X-1: [Strohmayer & Mushotzky \(2003\)](#) used an *XMM-Newton* observation, and reported an EW of 230–1300 eV depending on spectral fitting model; an EW of 30–80 eV was reported by [Caballero-García \(2011\)](#), who used a *Suzaku* observation. Up to now, the iron line in NGC 7456 ULX-1 has the highest EW ever detected in ULX sources. The data above 10 keV with high spacial resolution is necessary to confirm if the line originates in disk reflection; however, both the low flux and ultraluminous soft spectral state of NGC 7456 ULX-1 make the source a poor candidate for a *NuSTAR* observation.

NGC 7456 ULX-1 has 0.3–10 keV  $F_{\text{var}} = 44.25 \pm 1.46\%$  over time scales of 1000 s to 40 ks. This is the highest short term variability amplitude measured in ULXs so far. We found that the disk component varies little, but the emission above 1 keV is increasingly variable.

Our timing analysis of NGC 7456 ULX-1 indicates the source is variable on ks time scales, and we detected the soft X-ray band lagging behind the hard X-ray band with a  $\sim 1300$  s delay at 0.1 mHz. The covariance spectrum of NGC 7456 ULX-1 follows the shape of the harder spectral component and there is a clear lack of a soft excess, similar to other variable ULXs ([Middleton et al. 2015](#)). The lack of variability in the softer component suggests it plays no role in generating the soft X-ray lag. Furthermore, the high coherence between the soft and hard bands means there is a single driver of the variability. Together these are consistent with the soft lag being intrinsic to the harder component and not being a delay between the two spectral components. In the other words the harder component shows the rapid variability and the low energy photons of this component arrive over a ks later than the high energy photons.

NGC 7456 ULX-1 would be the fifth ULX source to exhibit a soft lag. A high frequency soft X-ray lag in a ULX was first detected in NGC 5408 X-1 by [Heil & Vaughan \(2010\)](#) and later by [De Marco et al. \(2013b\)](#) and [Hernández-García et al. \(2015\)](#). Later, a soft X-ray lag was detected in NGC 55 ULX1 ([Pinto et al. 2017](#)), NGC 1313 X-1 ([Kara et al. 2020](#)) and recently in NGC 4559 X7 ([Pintore et al. 2021](#)). In Fig. 8 we plot the unabsorbed 0.3–10 keV X-ray luminosity versus soft lag amplitude of ULXs detected in similar energy bands. NGC 55 ULX1 and NGC 7456 ULX-1 show nearly the same lag amplitude in a similar frequency interval. NGC 1313 X-1 and NGC 4559 X7 show a somewhat shorter lag, but in a higher frequency interval. Given the similar amplitudes, it is possible that the soft lag in these four sources have the same physical origin. On the other hand, the lag amplitude in 5408 X-1 is an order of magnitude smaller. The different behaviour of NGC 5408 X-1 may be due to the soft lag in this source having a different origin from the other ULXs. [De Marco et al. \(2013b\)](#) measured the soft X-ray lag in NGC 5408 X-1 with amplitude of  $\sim 5$  s on the time scale 5–20 mHz. Furthermore,

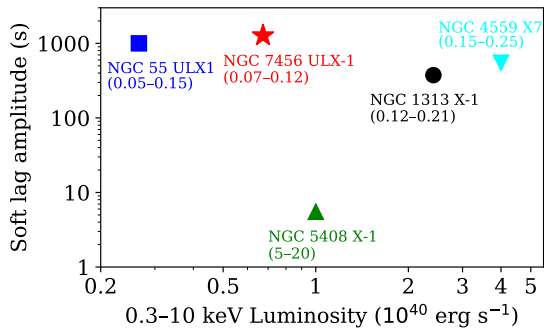


**Figure 8.** The lag amplitude of NGC 7456 ULX-1 compared with the lag amplitudes discovered in other ULXs: NGC 55 ULX1 (Pinto et al. 2017), NGC 5408 X-1 (De Marco et al. 2013b), NGC 1313 X-1 (Kara et al. 2020) and NGC 4559 X7 (Pintore et al. 2021). The number in parenthesis indicates the frequency range in mHz where the soft lag is detected.

Hernández-García et al. (2015) extended the analysis to longer time scales. The authors found a longer soft lag amplitude of  $\sim 100$  s at  $\sim 0.35$  mHz but not long enough to be comparable to the other four ULXs. Moreover at even lower frequencies, around 0.1 mHz, Hernández-García et al. (2015) observed a hard lag. So, it is clear that NGC 5408 X-1 is an outlier, relative to the other four sources.

The soft X-ray lag in AGN is well established and the explanation for its origin is thought to be due to light travel time delays between the primary coronal emission and the reprocessed emission (reverberation) in the accretion disk within roughly  $10r_g$  of the central BH (De Marco et al. 2013a). If the lag in NGC 7456 ULX-1 is really due to reverberation from the inner region of the accretion disk, the  $\sim 1300$  s delay would imply a BH mass of  $\sim 10^7 M_{\odot}$ , which is extremely high. The other explanation could be that reflection of the primary X-ray occurs at larger distances from the central compact object. If we consider that NGC 7456 ULX-1 is a stellar or intermediate mass BH of  $10-10^4 M_{\odot}$ , then the reverberation must be originating from  $\sim 10^7-10^4 r_g$ , which is consistent with a distant reflector. Furthermore, the lack of soft excess in the covariance spectra (see Uttley et al. 2011 for the soft excess in covariance spectra of GX 339-4) makes the reverberation model to be highly unlikely for possible explanation of the soft X-ray lag origin in NGC 7456 ULX-1.

From variability studies of ULXs it has been found that soft ULXs show more variability than hard ULXs and the variability is strongest at higher energies (Sutton et al. 2013). This is often explained under the scenario that the soft ULXs are seen through outflowing wind material which intermittently blocks our line of sight to the hot central region. Therefore the softer photons come from the down scattering of hard photons. This leads to a higher flux in the softer band so the source appears as a soft ULX and the intermittent blocking of hard photons by the wind leads to large variability at higher energies. This picture perfectly fits into the case of NGC 7456 ULX-1. The origin of the soft lag could be explained in a similar picture. In such a picture the absorption opacity of the material should be low for high energy photons and high for low energy photons. So the low energy photons of the harder component go through a large number of scatterings into optically thick wind, compared to the high energy photons. This will introduce a long delay between the arrival times of low and high energy photons of the harder component and the lag amplitude will give the extent of the outflow. However absorption may decrease the coherence (e.g. De Marco et al. 2020), particularly if the wind has a high column density and/or low ionization. On the contrary, we measure a high coherence for NGC 7456 ULX-1 (Fig. 5).

## 5 ACKNOWLEDGEMENTS

AR was partially supported by Polish National Science Center grants No. 2015/17/B/ST9/03422 and 2015/18/M/ST9/00541. BDM acknowledges support from Ramón y Cajal Fellowship RYC2018-025950-I. AGM was partially supported by Polish National Science Center grants 2016/23/B/ST9/03123 and 2018/31/G/ST9/03224.

## 6 DATA AVAILABILITY

The data is publicly available from ESA’s XMM-Newton Science Archive and NASA’s HEASARC archive.

## REFERENCES

- Akaike H., 1974, *IEEE Transactions on Automatic Control*, **19**, 716
- Arnaud K. A., 1996, *XSPEC: The First Ten Years*. p. 17
- Bachetti M., et al., 2014, *Nature*, **514**, 202
- Brightman M., et al., 2018, *Nature Astronomy*, **2**, 312
- Caballero-García M. D., 2011, *MNRAS*, **418**, 1973
- Carpano S., Haberl F., Maitra C., Vasilopoulos G., 2018, *MNRAS*, **476**, L45
- De Marco B., Ponti G., Cappi M., Dadina M., Uttley P., Cackett E. M., Fabian A. C., Miniutti G., 2013a, *MNRAS*, **431**, 2441
- De Marco B., Ponti G., Miniutti G., Belloni T., Cappi M., Dadina M., Muñoz-Darias T., 2013b, *MNRAS*, **436**, 3782
- De Marco B., et al., 2020, *A&A*, **634**, A65
- Earnshaw H. M., et al., 2016, *MNRAS*, **456**, 3840
- Edelson R., Turner T. J., Pounds K., Vaughan S., Markowitz A., Marshall H., Dobbie P., Warwick R., 2002, *ApJ*, **568**, 610
- Fürst F., et al., 2016, *ApJ*, **831**, L14
- Gladstone J. C., Roberts T. P., Done C., 2009, *MNRAS*, **397**, 1836
- Heil L. M., Vaughan S., 2010, *MNRAS*, **405**, L86
- Heil L. M., Vaughan S., Roberts T. P., 2009, *MNRAS*, **397**, 1061
- Hernández-García L., Vaughan S., Roberts T. P., Middleton M., 2015, *MNRAS*, **453**, 2877
- Houck J. C., Denicola L. A., 2000, in Manset N., Veillet C., Crabtree D., eds, *Astronomical Society of the Pacific Conference Series Vol. 216*, *Astronomical Data Analysis Software and Systems IX*. p. 591
- Israel G. L., et al., 2017a, *Science*, **355**, 817
- Israel G. L., et al., 2017b, *MNRAS*, **466**, L48
- Jansen F., et al., 2001, *A&A*, **365**, L1
- Kaastra J. S., Bleeker J. A. M., 2016, *A&A*, **587**, A151
- Kara E., et al., 2020, *MNRAS*, **491**, 5172
- Middleton M. J., Heil L., Pintore F., Walton D. J., Roberts T. P., 2015, *MNRAS*, **447**, 3243
- Mondal S., Różańska A., Lai E. V., De Marco B., 2020, *A&A*, **642**, A94
- Mondal S., Rozanska A., Baginska P., Markowitz A., De Marco B., 2021, *arXiv e-prints*, p. [arXiv:2104.12894](https://arxiv.org/abs/2104.12894)
- Pinto C., et al., 2017, *MNRAS*, **468**, 2865
- Pintore F., et al., 2020, *ApJ*, **890**, 166
- Pintore F., et al., 2021, *MNRAS*,
- Rodríguez Castillo G. A., et al., 2020, *ApJ*, **895**, 60
- Sathyaprakash R., et al., 2019, *MNRAS*, **488**, L35
- Schwarz G., 1978, *Annals of Statistics*, **6**, 461
- Strohmer T. E., Mushotzky R. F., 2003, *ApJ*, **586**, L61
- Sutton A. D., Roberts T. P., Middleton M. J., 2013, *MNRAS*, **435**, 1758
- Timmer J., Koenig M., 1995, *A&A*, **300**, 707
- Tully R. B., Courtois H. M., Sorce J. G., 2016, *AJ*, **152**, 50
- Uttley P., Wilkinson T., Cassatella P., Wilms J., Pottschmidt K., Hanke M., Böck M., 2011, *MNRAS*, **414**, L60
- Uttley P., Cackett E. M., Fabian A. C., Kara E., Wilkins D. R., 2014, *A&ARv*, **22**, 72
- Vaughan B. A., Nowak M. A., 1997, *ApJ*, **474**, L43
- Vaughan S., Edelson R., Warwick R. S., Uttley P., 2003, *MNRAS*, **345**, 1271
- Walton D. J., Roberts T. P., Mateos S., Heard V., 2011, *MNRAS*, **416**, 1844
- Wilkinson T., Uttley P., 2009, *MNRAS*, **397**, 666